

from all extant models have large uncertainties because changes in ice marginal position, accumulation rate, and effective ice softness are poorly known. Our thickness history is consistent with the detailed layer thickness analysis of Bolzan *et al.* (26). However, we cannot be confident that this thickness increase implies a greater climatic temperature change, because the difference between cloud and surface temperatures also may have changed.

37. W. S. Broecker and G. H. Denton, *Geochim. Cosmochim. Acta* **53**, 2465 (1989).

38. Fossil and other data are reviewed by region in H. E. Wright *et al.*, Eds., *Global Climates since the Last Glacial Maximum* (Univ. of Minnesota Press, Minneapolis, 1993).

39. M. Stute *et al.*, *Science* **269**, 379 (1995).

40. J. W. Beck *et al.*, *ibid.* **257**, 644 (1992); T. P. Guilderson, R. G. Fairbanks, J. L. Rubenstone, *ibid.* **263**, 663 (1994).

41. Estimates of the tropical glacial-Holocene warming based on planktonic microfossil assemblages are

considerably smaller [CLIMAP Project Members, *Geol. Soc. Am. Map Chart Ser. MC-36* (1981); (40)]. This discrepancy is not resolved, but a wider variety of evidence indicates $\sim 5^{\circ}\text{C}$ of warming.

42. Interpretation of borehole temperature data from Dye 3 must include strong horizontal heat advection, which has probably changed through time, and larger uncertainties in the accumulation history compared to GISP2. The GISP2 core has shown the glacial accumulation rate to be approximately one-third that of the Holocene (24). For this accumulation rate contrast, two analyses of Dye 3 temperature (16, 44) indicate an approximately 14°C deglacial temperature change.

43. For summary, see J. T. Houghton, G. J. Jenkins, J. J. Ephraums, Eds., *Climate Change: The IPCC Scientific Assessment* (Cambridge Univ. Press, Cambridge, 1990).

44. J. Firestone, *J. Glaciol.* **41**, 39 (1995).

45. Our filter is the resolution kernel of Backus-Gilbert inversion; W. Menke, *Geophysical Data Analysis:*

Discrete Inverse Theory (Academic Press, San Diego, revised ed., 1989), pp. 71–72.

46. N. S. Gundestrup, D. Dahl-Jensen, S. J. Johnsen, A. Rossi, *Cold Reg. Sci. Tech.* **21**, 399 (1993); analyses pending (D. Dahl-Jensen and S. Johnsen, in preparation).

47. For the “no north-south spreading,” we assumed that the ice flow is two-dimensional (east-west and vertical). The uncorrected accumulation rate history has not been corrected for thickness changes of the ice sheet. For “no fabric evolution,” there is no enhancement of ice softness for ice deposited during glacial times.

48. This work was supported by the NSF (some material is based on work supported by a NSF Graduate Research Fellowship) and the U.S. Geological Survey. We thank the GISP2 Science Management Office, the 109th Air National Guard, the Polar Ice Coring Office, and GISP2 participants.

31 May 1995; accepted 18 August 1995

Superplasticity in Earth's Lower Mantle: Evidence from Seismic Anisotropy and Rock Physics

Shun-ichiro Karato,* Shuqing Zhang, Hans-Rudolf Wenk

In contrast to the upper mantle, the lower mantle of the Earth is elastically nearly isotropic, although its dominant constituent mineral [(Mg,Fe)SiO₃ perovskite] is highly anisotropic. On the basis of high-temperature experiments on fabric development in an analog CaTiO₃ perovskite and the elastic constants of MgSiO₃ perovskite, the seismic anisotropy was calculated for the lower mantle. The results show that absence of anisotropy is strong evidence for deformation by superplasticity. In this case, no significant transient creep is expected in the lower mantle and the viscosity of the lower mantle is sensitive to grain size; hence, a reduction in grain size will result in rheological weakening.

Rheological properties have an important influence on the nature of flow in the deep interior of the Earth, but both laboratory and theoretical studies of deep mantle rheology have significant limitations. Quantitative measurements of the strength of materials under high pressures and temperatures are difficult, and no rheological measurements have been performed under lower mantle conditions. Neither the rheological constitutive relation (that is, the dependence of viscosity on stress or grain size or both) nor the absolute values of viscosity of the lower mantle are well constrained (1). The rheology of the Earth's deep interior can be inferred from laboratory data only after a large extrapolation in time scales, which introduces a significant amount of uncertainty. Similarly, theoretical estimates of rheological properties of the Earth's deep interior from time-dependent deformation are difficult to make because of (i) the poor sensitivity of the data to rheo-

logical properties of the deep portions of the Earth (2), (ii) the uncertainties in some key input parameters such as the melting history of ice sheets (3) in the analysis of the postglacial rebound, or (iii) the density-to-velocity conversion factor (4) in the analysis of the geoid.

One strategy to get around these difficulties is to combine seismological observations of anisotropy and laboratory studies of deformation-induced lattice preferred orientation [for example (5)]. The anisotropic structure of deformed materials depends on deformation mechanisms (and deformation geometry) [for a review, see (6)], and anisotropic structures can be observed seismologically as far down as the center (that is, inner core) of the Earth (7). Plastic deformation by diffusion or superplastic creep will result in an isotropic structure, whereas deformation by dislocation creep or twinning results in an anisotropic structure. Thus, although this approach will not provide direct estimates of the absolute values of viscosities, it provides information as to the rheological constitutive relation (stress or grain-size dependence of viscosity) and hence indirectly indicates rheological discontinuities or weakening associated with

grain-size reduction (5, 8).

Here we apply this strategy to the lower mantle. One of the most striking observations of the lower mantle is the absence of significant seismic anisotropy (9) even though the dominant mineral in the lower mantle, orthorhombic (Mg,Fe)SiO₃ perovskite, has significant elastic anisotropy (10, 11). The absence of observed anisotropy in the lower mantle could be attributed to (i) chaotic convection; (ii) limited plastic deformation; (iii) the anisotropic structure in the lower mantle which happens to be such that, for seismic waves traveling nearly vertically [such as those used in seismological studies (9)], the amount of shear wave splitting is small (12); or (iv) the fact that the deformation does not result in an anisotropic structure. The first hypothesis means that the lower mantle materials could have anisotropic structure (possibly due to deformation by dislocation creep), but the scale of coherent deformation is much smaller than the length of typical seismic wave paths (for ScS or SKS) so that, on average, no appreciable anisotropy would be detected. This hypothesis is unlikely because seismic tomography indicates that the lower mantle structure is dominated by long wave length features (13), and a high viscosity of the lower mantle will make chaotic convection difficult to achieve (14). The second hypothesis is also untenable because seismic tomography indicates the presence of downgoing and upwelling currents in the lower mantle (15), and the Rayleigh number for the lower mantle is likely to exceed the critical value [see, for example, (1)]. Discrimination of the last two alternatives requires an investigation of the relation between the nature of deformation and seismic anisotropy in lower mantle materials.

The most direct data on this subject must ultimately come from high-pressure, high-temperature deformation experiments performed on polycrystalline (Mg,Fe)SiO₃

S.-i. Karato and S. Zhang, Department of Geology and Geophysics, University of Minnesota, Minneapolis, MN 55455, USA.

H.-R. Wenk, Department of Geology and Geophysics, University of California, Berkeley, CA 94720, USA.

*To whom correspondence should be addressed.

perovskites. However, these experiments cannot be done with current technology. Meade *et al.* studied the preferred orientation of (Mg,Fe)SiO₃ perovskite under lower mantle pressures and at room temperature (16). However, as deformation mechanisms at the room temperatures used in their study are not likely to be the same as those operating at the high temperatures of the lower mantle, the relevance of their results to the seismic anisotropy in the lower mantle is not clear.

In our study, we used an analog material, CaTiO₃, to gain insight into the geodynamical implications of the observed seismic isotropy of the lower mantle. Use of an analog material is suitable in the study of deformation fabrics (the preferred orientation of crystals) which are mainly determined by the nature of slip systems and twinning that in turn are primarily controlled by crystal structure. CaTiO₃ is considered to be a good analog because most of the defect-related features that control the preferred orientation are similar to the features found in (Mg,Fe)SiO₃ perovskite (17). Karato *et al.* (18) found that diffusion creep dominates in CaTiO₃ perovskite under a wide range of conditions, and they suggested that diffusion creep might be a dominant mechanism of flow in the lower mantle. On the basis of these results, we prepared polycrystalline CaTiO₃ with different grain sizes (~8 μm and ~70 μm in diameter) and deformed them to large shear strains (up to ~300%) using a technique described in (19). The sample with ~8-μm grain size was deformed in the diffusion creep regime, and the other sample with ~70-μm grain size was deformed in the dislocation creep regime. We chose this mode of deformation because the likely deformation geometry in the mantle is simple shear rather than axial compression (20) and because the large strains necessary for texture studies will be easily achieved in this geometry but not in axial compression. The deformation conditions were *P* (pressure) = 300 MPa and *T* (temperature) = 1498 K (which is equal to 0.68 *T_m*, where *T_m* is the melting temperature), and $\dot{\epsilon}$ (shear strain rate) ranged from 0.7×10^{-5} to $18 \times 10^{-5} \text{ s}^{-1}$ up to ~310% strain (21).

The fine-grained samples typically showed homogeneous deformation, whereas the coarse-grained specimens showed some heterogeneous deformation caused by dynamic recrystallization in which relict grains show a large elongation but newly formed recrystallized grains remain nearly equant shape. The coarse-grained samples showed somewhat asymmetrical grain shapes, often referred to as fish (22), which presumably result from the deformation of fine-grained recrystallized grains (Fig. 1A). In contrast, almost all the grains in the

fine-grained specimens showed nearly equant shapes despite large strain (Fig. 1B). These observations, together with the observed small stress exponent [$\dot{\epsilon} \sim \sigma$, where σ is stress (18)] and grain-size sensitivity at

small grain sizes [$\dot{\epsilon} \sim 1/d^2$, where *d* is grain size (18)], imply that deformation in the fine-grained specimens was by superplasticity, where grain boundary sliding contributes significantly to strain (23).

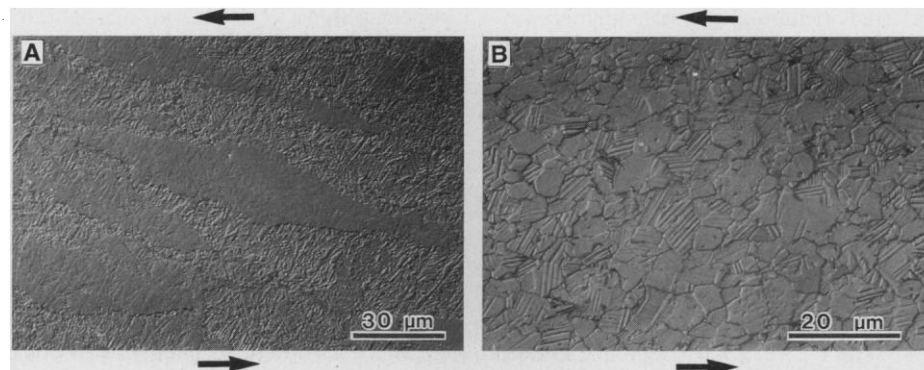


Fig. 1. Microstructures of deformed CaTiO₃ perovskite. Optical micrographs of polished sections after chemical etching taken with reflected light (with Nomarsky contrast). **(A)** A coarse-grained sample deformed in the dislocation creep regime [*P* = 300 MPa, *T* = 1498 K, $\dot{\epsilon}$ (shear strain rate) = $18 \times 10^{-5} \text{ s}^{-1}$, and ϵ (shear strain) = 310%]. **(B)** A fine-grained sample deformed in the superplastic regime (*P* = 300 MPa, *T* = 1498 K, $\dot{\epsilon}$ = $4 \times 10^{-5} \text{ s}^{-1}$, and ϵ = 173%). Grain shape changes in the coarse-grained specimen follow approximately the strain ellipsoid. In contrast, almost no grain elongation is found in the fine-grained specimen. Numerous twin boundaries are seen in both specimens. Shear direction is east-west, and the sense of shear is indicated by arrows.

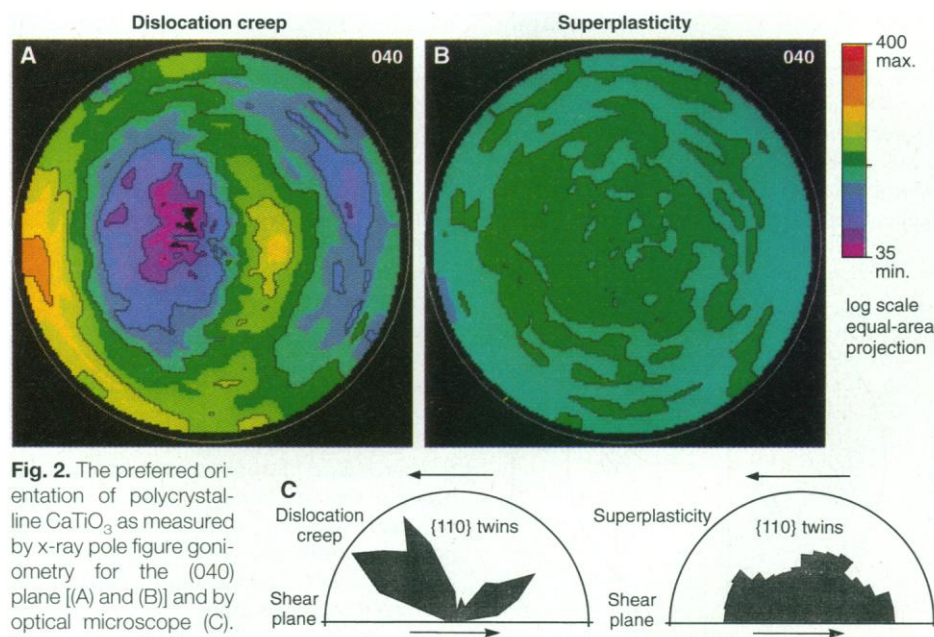


Fig. 2. The preferred orientation of polycrystalline CaTiO₃ as measured by x-ray pole figure goniometry for the (040) plane [(A) and (B)] and by optical microscope (C). The x-ray pole figures are plotted on the shear plane by using the upper hemisphere projection. The color-coded pole densities are related to a logarithmic scale that expresses pole densities in 100× multiples of a random distribution [a value of 100 (that is, green) means that the pole distribution is random]. **(A)** A coarse-grained sample deformed in the dislocation creep regime (*T* = 1498 K, $\dot{\epsilon}$ = $18 \times 10^{-5} \text{ s}^{-1}$, and ϵ = 310%). **(B)** A fine-grained specimen deformed in the diffusion creep (superplastic) regime (*T* = 1498 K, $\dot{\epsilon}$ = $5 \times 10^{-5} \text{ s}^{-1}$, and ϵ = 30%). Note the strong preferred orientation in the coarse-grained specimen and very weak preferred orientation in the fine-grained specimen. The strength of preferred orientation reaches nearly steady state at strains of ~50 to 70% in the dislocation creep regime; therefore, a large difference in the strength of preferred orientation between two sets of specimens is due mainly to the difference in deformation mechanisms and not by the difference in the magnitude of strain. This point is demonstrated in **(C)** where the orientation of the {110} twin boundaries is plotted for the two samples (one deformed in the dislocation creep regime at *T* = 1498 K, $\dot{\epsilon}$ = $0.7 \times 10^{-5} \text{ s}^{-1}$, and ϵ = 30% and the other deformed in the superplasticity regime at *T* = 1498 K, $\dot{\epsilon}$ = $4 \times 10^{-5} \text{ s}^{-1}$, and ϵ = 173%). The plots are on the plane perpendicular to the shear plane. About 2000 twin boundaries were measured.

We measured the fabric (lattice preferred orientation) of deformed samples using both an optical microscope equipped with a universal stage and an x-ray pole figure goniometer (Fig. 2) (24). Again, marked contrasts were found between fine-grained and coarse-grained specimens. The preferred orientation in coarse-grained samples was strong; the *a* axis became subparallel to the flow direction and the *b* axis perpendicular to the flow plane. In contrast, fine-grained specimens showed almost random preferred orientation, consistent with the absence of preferred orientation in superplastically deformed metals (23).

On the basis of the preferred orientation of individual grains measured with a universal stage, we calculated seismic wave velocities using the elastic constants of MgSiO_3 perovskite (11, 25) and the program developed by Mainprice (26) (Fig. 3). For the ScS wave, whose pass length in the lower mantle is ~ 4000 km (~ 2000 km for SKS), the expected shear wave splitting for dislocation creep ranges from ~ 1 to ~ 36 s (0.5 to 18 s for SKS) depending on the geometry of flow. The observed small shear wave splitting (less than 0.2 s) is marginally consistent with a horizontal flow, but we consider that a horizontal flow is unlikely at least in the areas where shear wave splitting was studied (27). For a vertical flow, we expect shear wave splitting of ~ 20 s (~ 10 s for SKS), which is much larger than the observed values (less than 0.2 s). The preferred orientation in samples deformed by superplastic creep is much smaller; hence, weaker seismic anisotropy results (28).

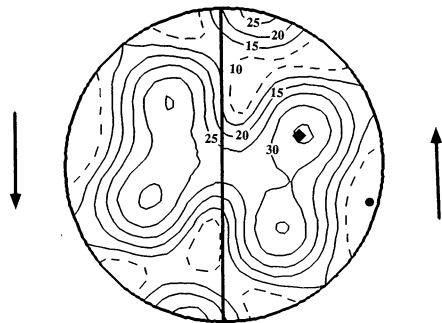


Fig. 3. Shear wave splitting of a perovskite aggregate deformed by dislocation creep, calculated from the preferred orientation of a coarse-grained CaTiO_3 and the elastic constants of MgSiO_3 perovskite. The magnitude of shear wave splitting is plotted on a plane perpendicular to the shear plane including the shear direction. The sense of shear is indicated by arrows. For vertical shear with a layer ~ 4000 km (~ 2000 km) thick, the flow direction is nearly parallel to the [100]-axis peak, and the expected shear wave splitting will be ~ 30 s (~ 15 s). For a superplastically deformed perovskite, the shear wave splitting is much smaller. ■, maximum of 36 S; ●, minimum of 1 s. Path length is 4000 km.

Therefore, we conclude that the observed small shear wave splitting in the lower mantle suggests that deformation there is by superplastic flow.

We have assumed that seismic anisotropy in the lower mantle is determined solely by that of perovskite. The secondary component, $(\text{Mg,Fe})\text{O}$, is also anisotropic (26), and it may contribute to shear wave splitting. We suggest that the absence of shear wave splitting in the lower mantle implies that $(\text{Mg,Fe})\text{O}$, if anything, should also deform by superplasticity.

Superplasticity is an important mechanism of deformation only under limited conditions. In particular, grain size must be maintained to be reasonably small (23). It is conceivable that a small grain size in the lower mantle is maintained by the presence of $(\text{Mg,Fe})\text{O}$; otherwise, grain growth would result in deformation by dislocation creep.

There is strong evidence that deformation is by dislocation creep in the upper portions of the upper mantle (5). Thus, the rheological constitutive relation (that is, the dependence of viscosity on stress or grain size) is different between the upper and lower mantle. Viscosity in the superplasticity regime strongly depends on grain size. Therefore, a reduction of grain size in the lower mantle will result in significant rheological weakening (18, 29). Also, the depth variation in viscosity of the lower mantle will depend on the depth variation in grain size. There will be no significant transient creep in the lower mantle. Thus, the rheology of the lower mantle inferred from the postglacial rebound will be free from the effects of transient creep and, therefore, should be identical to that estimated from geoid anomalies.

Effects of changes in rheological constitutive law on mantle convection could cause intermittent upwelling plumes from the boundary (30). Grain-size reduction associated with the phase transformation to the perovskite plus magnesiowustite assembly near the 660 km discontinuity will significantly weaken a subducted slab that penetrates into the lower mantle, which may cause it to deform or thicken, as has been seen in some seismic tomography (15).

REFERENCES AND NOTES

1. W. R. Peltier, in *Mantle Convection*, W. R. Peltier, Ed. (Gordon and Breach, New York, 1989), pp. 389–478; M. Nakada and K. Lambeck, *Geophys. J. Int.* **96**, 497 (1989); S. Karato, *Phys. Earth Planet. Inter.* **55**, 234 (1989).
2. J. X. Mitrovica and W. R. Peltier [*Geophys. J. Int.* **104**, 267 (1991)] showed that the current data set of relative sea levels has little sensitivity to the rheological structures of the mantle below ~ 1200 km.
3. K. Lambeck and M. Nakada, *Nature* **357**, 125 (1992); W. R. Peltier, *Science* **265**, 195 (1994).
4. Theoretical analysis of geoid anomalies requires data on density anomalies in the Earth which could be estimated from the anomalies of seismic wave velocities.

A. M. Forte, A. M. Dziewonski, and R. L. Woodward [in *Dynamics of Earth's Deep Interior and Earth Rotation*, J.-L. Mouli, D. E. Smylie, T. Herring, Eds. (American Geophysical Union, Washington, DC, 1993), pp. 135–166] inferred that this conversion factor changes significantly with depth. S. Karato [*Geophys. Res. Lett.* **20**, 1623 (1993)] showed that this conversion factor depends on depth through the depth variation of anelastic relaxation.

5. S. Karato and P. Wu, *Science* **260**, 771 (1993).
6. S. Karato, in *Rheology of Solids and of the Earth*, S. Karato and M. Toriumi, Eds. (Oxford Univ. Press, Oxford, 1989), pp. 393–422.
7. D. L. Anderson, *Theory of the Earth* (Blackwell, New York, 1989), chap. 15.
8. D. C. Rubie, *Nature* **308**, 550 (1984).
9. P. G. Silver, S. Kaneshima, and C. Meade [*Eos* **74**, 313 (1993)] estimated the shear wave splitting from the lower mantle by comparing the splitting from the direct S waves from the source to the station with the splitting of the shear waves that are refracted (SKS) or reflected (ScS) from the liquid core. The results indicate a weak shear wave splitting, less than 0.2 s, which indicates that the magnitude of anisotropy in the lower mantle is less than $\sim 1/100$ of that of the upper mantle.
10. The dominant mineral of the lower mantle is $(\text{Mg,Fe})\text{SiO}_3$ perovskite [see, for example, A. E. Ringwood, *Geochim. Cosmochim. Acta* **55**, 2083 (1991)]. Both experimental [N. Funamori and T. Yagi, *Geophys. Res. Lett.* **20**, 387 (1993)] and theoretical [L. Stixrude and R. E. Cohen, *Nature* **364**, 613 (1993); R. M. Wentzcovitch, J. L. Martins, G. D. Price, *Phys. Rev. Lett.* **70**, 3947 (1993)] studies indicate that the perovskite $[(\text{Mg,Fe})\text{SiO}_3]$ assumes an orthorhombic structure in most of the lower mantle conditions, although structural phase transformations to tetragonal or cubic (or some other unknown) structure might occur in the limited portions [G. H. Wolf and M. S. T. Bukowski, in *High-Pressure Research in Mineral Physics*, M. H. Manghnani and Y. Syono, Eds. (Terra Publications Tokyo/American Geophysical Union, Washington, DC, 1987), pp. 313–331; Y. Wang, F. Guyot, R. C. Liebermann, *J. Geophys. Res.* **97**, 12327 (1992); C. Meade, H.-K. Mao, J. Hu, *Science* **268**, 1743 (1995)]. Because a significant portion of the lower mantle is likely to be occupied with an orthorhombic perovskite, the use of elastic constants and lattice preferred orientation for orthorhombic perovskite is justified as a first approximation. When the crystal structure changes to other symmetries, then both lattice preferred orientation and elastic constants will change, and as a result, the elastic anisotropy will also change. But some seismic anisotropy is expected in the dislocation creep regime because of a significant lattice preferred orientation due to anisotropic dislocation glide [for anisotropy in dislocation creep in cubic perovskite, see Z. Wang, S. Karato, K. Fujino, *Phys. Earth Planet. Inter.* **79**, 299 (1993)]. However, no appreciable effect is expected in the superplastic regime where no lattice preferred orientation will occur.
11. A. Yageneh-Haeri, D. J. Weidner, E. Ito, *Science* **243**, 787 (1989).
12. There are some specific crystallographic orientations along which the shear wave splitting in perovskite is very small [for example, along the [010] orientation (11)]. This means that if these orientations are nearly vertical in the lower mantle, then one will observe a small shear wave splitting, although anisotropy of P wave velocities will be significant.
13. T. Tanimoto, *J. Phys. Earth* **38**, 493 (1990); W. Su and A. M. Dziewonski, *Nature* **352**, 121 (1991).
14. P. E. van Keken, D. A. Yuen, A. P. van den Berg, *Science* **264**, 1437 (1994).
15. Y. Fukao, M. Obayashi, H. Inoue, M. Nishii, *J. Geophys. Res.* **97**, 4809 (1992); S. P. Grand, *ibid.* **99**, 11591 (1994).
16. C. Meade, P. G. Silver, and S. Kaneshima [*Geophys. Res. Lett.* **22**, 1293 (1995)] reported results of room temperature and high-pressure deformation experiments of $(\text{Mg,Fe})\text{SiO}_3$ perovskite as well as olivine and CaTiO_3 . They found no significant lattice preferred orientation (LPO) in $(\text{Mg,Fe})\text{SiO}_3$ perovskite after a significant strain ($\sim 75\%$) under these conditions and discussed the idea that the preferred orientation under

- higher temperatures in the lower mantle would be smaller. The physical basis for this argument is weak, however, because the nature of LPO is closely related to the geometry of slip systems and of twinning which is sensitive to temperatures, and there is no general relation between LPO and temperatures. In fact, less LPO is found under lower temperatures in olivine because of the complexities of the active slip systems [A. Nicolas and N. I. Christensen, in *Composition, Structure and Dynamics of the Lithosphere/Asthenosphere System*, K. Fuchs and C. Froidevaux, Eds (American Geophysical Union, Washington, DC, 1987), pp. 111–123]. This trend in olivine is inconsistent with the observation of Meade *et al.* and suggests that mechanisms other than dislocation glide (for example, fracturing) are responsible for the LPO observed in these experiments.
17. Defect-related properties that control the preferred orientation of minerals include slip systems and twinning mechanisms [see, for example, P. van Houtte and F. Wagner, in *Preferred Orientation in Deformed Metals and Rocks: An Introduction to Modern Texture Analysis*, H.-R. Wenk, Ed. (Academic Press, New York, 1985), pp. 233–258], both of which are similar between CaTiO_3 and $(\text{Mg,Fe})\text{SiO}_3$ [N. Doukhan and J.-C. Doukhan, *Phys. Chem. Mineral.* **13**, 403 (1986); S. Karato, K. Fujino, E. Ito, *Geophys. Res. Lett.* **17**, 13 (1990); Y. Wang, thesis, State University of New York at Stony Brook (1991), p. 232].
 18. S. Karato and P. Li, *Science* **255**, 1238 (1992); P. Li, S. Karato, Z. Wang, *Phys. Earth Planet. Inter.*, in press.
 19. S. Zhang and S. Karato, *Nature* **375**, 774 (1995).
 20. Deformation in the lower mantle will be dominated by a vertical motion associated with upwelling or downgoing plumes except near the bottom (that is, the D'' layer) and a possible boundary layer near the 660 km discontinuity. Thus, the dominant mode of deformation in the lower mantle will be vertical shear to a first approximation.
 21. At this P - T condition, CaTiO_3 assumes an orthorhombic structure (space group $Pbnm$) that is the same as the structure of the $(\text{Mg,Fe})\text{SiO}_3$ perovskite under most lower mantle conditions (10). The homologous temperature (that is, T/T_m) in the lower mantle is similar to these conditions ($T/T_m = 0.6$ to 0.7 in the shallow lower mantle [A. Zerr and R. Boehler, *Science* **262**, 553 (1993)]. Under these conditions, a fine-grained ($\sim 8 \mu\text{m}$) CaTiO_3 will deform by diffusion (or superplastic) creep, whereas a coarse-grained ($\sim 70 \mu\text{m}$) counterpart will deform by dislocation creep (18).
 22. G. S. Lister and A. W. Snoke, *J. Struct. Geol.* **6**, 617 (1984).
 23. J. W. Edington, K. N. Melton, C. P. Cutler, *Prog. Mater. Sci.* **21**, 63 (1976).
 24. X-ray measurements of the orientation of (040) lattice planes were made for both coarse- and fine-grained specimens in reflection and transmission geometry. In optical measurements for coarse-grained specimens, the preferred orientation of all of the three crystallographic axes of individual grains was determined with the universal stage. This is not possible to do for fine-grained specimens, so we measured the orientation of the {110} twin boundaries on the polished and etched sections. About 2000 twin boundaries were measured.
 25. We used laboratory data on MgSiO_3 perovskite at ambient conditions. The effects of pressure and temperature on individual elastic constants in perovskite are not known, and neither are the effects of Fe, which might change the anisotropy. However, in the case of olivine, the temperature and pressure effects and also the effects of Fe on anisotropy are weak (7), so therefore we assume that the elastic anisotropy of perovskite in the lower mantle is similar to that measured at room pressure and temperature (11).
 26. D. H. Mainprice, *Comput. Geosci.* **16**, 385 (1990). In this calculation, the elastic constants of a single crystal of MgSiO_3 perovskite are used, and the anisotropic elastic properties of an aggregate are calculated from the orientation of individual grains by using the Voigt averaging scheme.
 27. Shear wave splitting was studied near subduction zones (9). Seismic tomography (15) and some numerical simulations [P. Tackley, D. J. Stevenson, G. A. Glazmaier, G. Schubert, *Nature* **361**, 699 (1993); S. Honda, D. A. Yuen, S. Balachandrar, D. Reuteler, *Science* **259**, 1308 (1993)] suggest that the dominant geometry of deformation in these regions is vertical shear.
 28. The seismic anisotropy for samples deformed by superplastic creep was not calculated because the complete crystallographic orientation of individual grains was measured only for coarse-grained samples deformed by dislocation creep. However, the nearly random orientation of grains found by x-ray measurements (Fig. 2) indicates that seismic anisotropy must be very weak.
 29. E. Ito and H. Sato, *Nature* **351**, 140 (1991).
 30. P. van Keken, D. A. Yuen, A. van den Berg, *Earth Planet. Sci. Lett.* **112**, 179 (1992); A. P. van den Berg, P. van Keken, D. A. Yuen, *Geophys. J. Int.* **115**, 62 (1993); P. van Keken, D. A. Yuen, A. van den Berg, *Geophys. Res. Lett.* **20**, 1927 (1993).
 31. We thank P. G. Silver and D. A. Yuen for discussions and D. H. Mainprice for sending the program to calculate the seismic anisotropy. Supported by grants from NSF to S.K. (EAR-9206683 and EAR-9220172).

30 May 1995; accepted 11 August 1995

Large-Scale Interplanetary Magnetic Field Configuration Revealed by Solar Radio Bursts

M. J. Reiner, J. Fainberg, R. G. Stone

An instantaneous view of the interplanetary extension of the solar magnetic field is provided here by measurements from a space platform at high ecliptic latitudes of the trajectories of individual type III solar radio bursts. The Ulysses spacecraft provides this unique vantage point with an orbit taking it far from the ecliptic plane. The Ulysses radio measurements illustrate the capability of detecting and tracking coronal disturbances as they propagate through the interplanetary medium.

Solar energetic processes, such as solar flares, inject energetic electrons into interplanetary space, where, as a result of their small gyroradii, these electrons are constrained to follow the interplanetary extension of the solar magnetic field. As the suprathermal electrons propagate through the interplanetary medium, they interact with the local plasma to generate radio emissions (1) at the plasma frequency and its harmonic (2). Because the plasma frequency (proportional to the square root of the solar wind plasma density) falls off with increasing heliocentric distance, radio emission generated farther from the sun occurs at lower frequencies. For radio emission generated from regions near the sun to near Earth's orbit at 1 astronomical unit ($1 \text{ AU} = 1.5 \times 10^8 \text{ km}$), the plasma frequency ranges from several hundreds of megahertz to $\sim 50 \text{ kHz}$; the precise values depend on the interplanetary conditions at the time of the radio emission and on whether the emission occurs at the fundamental or harmonic of the plasma frequency. Both direct observations (3, 4) and modeling (5) indicate that the radio emission is broadly beamed in the direction of the interplanetary magnetic field, but the value of the beamwidth is difficult to estimate. The radio manifestation of the interaction of the electrons with the solar wind as they propagate along the magnetic field lines through the interplanetary medium is known as a type III radio burst (6). Low-frequency type III radio bursts have been observed for de-

cares by spacecraft located in the ecliptic plane (7).

The Ulysses spacecraft, launched in October 1990, used the intense gravitational field of Jupiter to rotate its orbital plane far out of the ecliptic; it became the first spacecraft to go to high ecliptic latitudes and over the poles of the sun (8). During the southern polar pass, which occurred during September and October of 1994, Ulysses went as high as 80°S ecliptic latitude at a distance of $\sim 2 \text{ AU}$ below the ecliptic plane. After a rapid passage through the ecliptic plane ($\sim 1^\circ \text{ day}^{-1}$ in ecliptic latitude), Ulysses made a northern polar pass, reaching a maximum northern ecliptic latitude of 79°N in late August 1995. The instrumentation on Ulysses includes a sensitive radio receiver (9) with 76 discrete frequency channels covering the range from 1 to 940 kHz. This receiver is coupled to a 72.5-m (tip to tip) dipole antenna in the spin plane of the spacecraft and a 7.5-m monopole antenna along the spacecraft spin axis. During the in-ecliptic phase of the Ulysses mission, thousands of type III radio bursts were observed by this instrument. The Ulysses radio experiment was designed to determine the direction of arrival of the radiation from the measured modulation in the radio signals as the spacecraft spins about its axis (10). Ulysses observations therefore permit tracking of type III radio sources through interplanetary space.

During its trajectory to high latitudes, Ulysses continued to observe type III radio emission (11). This observation is significant because solar active regions, from

M. J. Reiner, Hughes STX, Lanham, MD 20706, USA.
J. Fainberg and R. G. Stone, NASA Goddard Space Flight Center, Greenbelt, MD 20771, USA.